Stability Criterion for Electrodeposition in Solid-State Batteries with Metallic Anodes

Yuanpeng Liu,[1,2,*] Jiawei Zhang,[1,2] Bowen Zhang,[1,2] Haowen Gao,[3] Dongjiang Chen,[4] Mingsheng Wang,[3,†] and Changguo Wang[1,2,‡]

[1] *Center for Composite Materials, Harbin Institute of Technology, Harbin, 150001, China*

[2] *National Key Laboratory of Science and Technology on Advanced Composites in Special Environments, Harbin Institute of Technology, Harbin 150080, China*

[3] *State Key Laboratory of Physical Chemistry of Solid Surfaces, College of Materials, Xiamen University, 361005 Xiamen, China*

[4] *State Key Laboratory of Electronic Thin Film and Integrated Devices, University of Electronic Science and Technology of China, Chengdu 610054, China*

(Received 6 July 2023; revised 19 December 2023; accepted 12 January 2024; published 21 February 2024)

We establish an analytical criterion for stable electrodeposition by combining electrochemistry and mechanics. *In situ* experiments combined with molecular simulations are performed to validate the robustness of the theoretical predictions. Our analysis shows that stable electrodeposition is intimately linked with the interfacial defect size, fracture toughness, and molar volume of solid electrolytes. We find an exponential scaling law between the critical current density and the interfacial defect size, and the inherent softening in strength of grain boundaries lowers the critical current density in polycrystalline solid electrolytes. Modeling and analyses provide roadmaps to design solid electrolytes with metallic anodes for achieving stable electrodeposition.

DOI: 10.1103/PRXEnergy.3.013010

I. INTRODUCTION

Electrodeposition, centuries-old technology for the fabrication of metallic thin films and coatings, has gained renewed scientific and technological interest due to its critical role in high-energy-density rechargeable batteries with metallic anodes [1,2]. However, charging such cells requires the electrodeposition of an active metal onto itself (e.g., Li, Na), a process that is inherently unstable [3–5]. Electrodeposition on the anode surface grows along the preferred orientation, ultimately leading to needlelike or mossylike morphologies, commonly known as dendrites [6,7]. Uncontrolled dendrite growth bridges the anode and cathode and results in an internal short circuit, leading to severe safety hazards for batteries. Thus, achieving stable electrodeposition is crucial for battery safety and performance promises, but so far there has been a lack of effective approaches [8–10].

Replacing conventional liquid electrolytes with solid electrolytes (SEs) is the most forward-looking route to block dendrite growth due to its high stiffness. Unfortunately, experiments show that dendrites are more easily formed in SE systems than in their liquid counterparts [11,12]. Taking lithium-based batteries as examples, the critical current density (CCD), above which lithium dendrites initiate and propagate, is 0.05−1.0 mA/cm^2 for garnet-type SEs and 0.1−0.4 mA/cm^2 for polyethylene oxide (PEO)-based SEs, whereas it can reach 4−10 mA/cm^2 for liquid electrolytes [13]. It is evident that there are distinct mechanistic differences in electrodeposition between solid and liquid electrolytes. The fundamental understanding of electrodeposition in solid-state cells remains insufficient [14–16].

Various factors influence the electrodeposition process in solid-based systems, such as the resistance of the anode-SE interface [17], interfacial geometry [18], electronic conductivity [19], microstructure [15], and the mechanical properties of the anode and SE [20]. In the absence of convincing experimental validation, it is unclear which factors are the most crucial for stable electrodeposition in metal-based batteries [21]. Recent observations show that the ubiquitous internal defects in solid-state systems, such

*liuyp@hit.edu.cn
†mswang@xmu.edu.cn
‡wangcg@hit.edu.cn

as grain boundaries, scratches, voids, or surface roughness, tend to become the "hot spots" for metal-atom deposition and even penetration [22–24], indicating a strong correlation between the interfacial void and unstable electrodeposition. These observations are very general and qualitatively similar findings have also been documented for Na/beta-Al systems [25]. This phenomenon stands in stark contrast to liquid-based systems, where the liquid hydrostatic pressure compels the electrolyte to permeate any interfacial voids, ensuring consistent contact. Without consideration of defect effects, the analysis will overestimate the blocking ability of SEs, and the predicted CCD is around 20 times larger than the experimental value [26,27]. Thus, identification of critical influencing factors and the establishment of criteria to accurately estimate stable electrodeposition are urgently needed [28–31].

This work aims to develop a general theory to quantitatively uncover the criterion for stable electrodeposition. We establish an analytical theoretical prediction of CCD, which is valid for both polymer and inorganic SEs. Our analysis correlates the condition for stable electrodeposition with the interfacial defect size, the fracture toughness and molar volume of SEs. Taking the $Li|Li_{6.4}La_3Zr_{1.4}Ta_{0.6}O_{12}$ (LLZO) Ta-doped cell as an example, the robustness of theoretical predictions is validated with the aid of *in situ* experiments and molecular simulations. The role of the grain boundary in electrodeposition is also discussed. The understanding uncovered in this work will have important implications for material selection and the interfacial design of SEs.

II. FORMULATION OF ELECTRODEPOSITION

Consider a metal-based battery system composing of a metal anode and a SE with a preexisting surface defect (e.g., cracks, scratch, voids), as shown in Fig. 1(a). Initially, the system is under relaxed state. Upon charging, metal ions (M^{z+}) from the electrolyte are reduced and deposited as new metal atoms (M), which can be expressed as $M^{z+} + ze^- \rightleftharpoons M$. Since defects are believed to act as preferential sites for electrodeposition [23], the new depositions preferentially fill the defect and form a protrusion into the SE [Fig. 1(b)].

To accommodate the newly deposited metal atoms, both the metal anode and the SE are pushed backward, leading to a field of stress at the interface. Mechanical stress resists deposition on the protrusion and slows down tip growth by decreasing the activation energy of the reaction. Thus, the interplay between electrochemistry and mechanics affects the electrodeposition process in solid-state batteries.

For simplicity, we consider a constant metal-ion concentration at the interface [32]. Based on the Butler-Volmer equation, the current density, i, can be expressed as

$$i = i_0 \left[\exp\left(-\alpha_a \frac{\mu_M - \mu_{M^{z+}} - z\mu_{e^-}}{RT} \right) - \exp\left(\alpha_c \frac{\mu_M - \mu_{M^{z+}} - z\mu_{e^-}}{RT} \right) \right], \quad (1)$$

where i_0 denotes the exchange current density; α_a and α_c are the anodic and cathodic charge transfer coefficients, satisfying $0 < \alpha_a < 1$ and $0 < \alpha_c < 1$, respectively [33]; F, R, and T are Faraday's constant, the ideal gas constant, and temperature, respectively; μ_M, $\mu_{M^{z+}}$, and μ_{e^-} represent the electrochemical potentials of the product (M) and reactants (M^{z+} and e^-) during electrodeposition, respectively. The whole electrochemical potential variation corresponding to the reaction kinetics can be recast as $\mu_M - \mu_{M^{z+}} - z\mu_{e^-} = \Delta\mu$, in which $\Delta\mu$ quantifies the additional potential change. It is known that $\Delta\mu$ is related to the local interfacial geometry [14], which plays a critical role in dendrite nucleation and growth.

To make the theory more tractable, it is widely accepted that the current density associated with the cathodic reaction can be negligible, since the anodic reaction dominates the reaction kinetics at the anode interface during electrodeposition [e.g., $\exp(\alpha_c(\mu_M - \mu_{M^{z+}} - z\mu_{e^-}/RT)) \ll \exp(-\alpha_a(\mu_M - \mu_{M^{z+}} - z\mu_{e^-}/RT))$] [34]. Thus, the new reaction kinetics relationship between the peak and valley of the defect can be expressed as

$$\frac{i_{peak}}{i_{valley}} = \exp\left(-\alpha_a \frac{\Delta\mu_{peak} - \Delta\mu_{valley}}{RT} \right), \quad (2)$$

where i_{peak}, i_{valley}, $\Delta\mu_{peak}$, and $\Delta\mu_{valley}$ are the current densities and the additional potential changes at the peak and valley of the defect, respectively. When $i_{peak}/i_{valley} \leq 1$, the electrodeposition rate at the peak is slower than that at the valley, so the protrusion tends to weaken or be invariable, resulting in stable electrodeposition [Fig. 1(c)]. When $i_{peak}/i_{valley} > 1$, the electrodeposition rate at the peak is faster than that at the valley, so the protrusion tends to largen, resulting in unstable electrodeposition [Fig. 1(d)]. Since $\alpha_a > 0$, the condition for stable electrodeposition requires

$$\Delta\mu_{peak} - \Delta\mu_{valley} \geq 0. \quad (3)$$

Different from liquid electrolytes, the additional potential change, $\Delta\mu$, in SEs is generally contributed by two parts: an electrochemically related potential change induced by a local electric field ($\Delta\mu^c$), and a mechanically related potential change induced by the deformation of the SE ($\Delta\mu^m$).

To obtain the closed-form criterion for stable electrodeposition, a cosine shape with amplitude a and half-wavelength b is adopted to describe the geometry of the

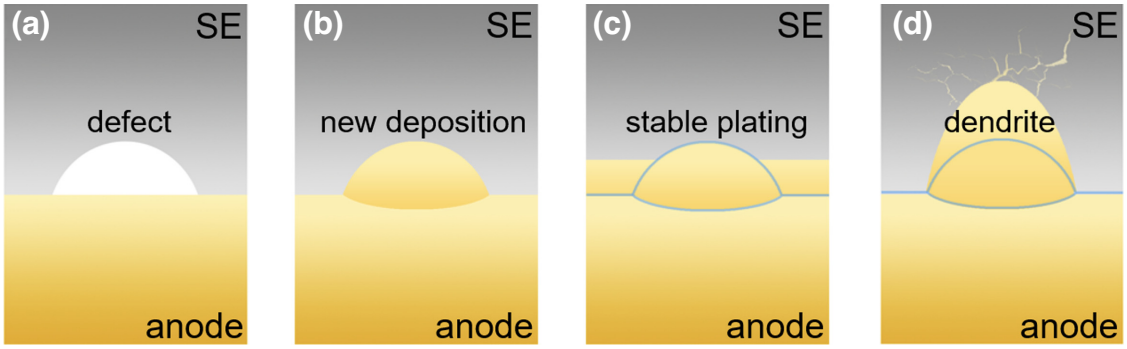

FIG. 1. Schematic of the process for electrodeposition. (a) Initial state with an interfacial defect. (b) New depositions fill the defect. (c) Stable electrodeposition. (d) Dendrite formation induced by unstable electrodeposition.

defect. A Cartesian coordinate system is located at the interface, as shown in Fig. 2. Under an applied electric field, E_0, lithium ions are driven to deposit at the interface. Due to the existence of the interfacial defect, excess electrons accumulate on the protrusion and create an amplified local electric field by drawing more metal ions around the peak of the defect. The difference in mass transport between the peak and valley induces a nonuniform overpotential, which, in turn, results in an electrochemical potential change.

In SEs, the distribution of electric potential is governed by the Laplace equation. By considering the generalized form of the Laplace equation and the axisymmetric nature of the applied electric field, the distribution of electric potential, φ, obeys the following law:

$$\varphi = E_0[y - X\exp(-Yy)\cos(Yx)] + Z, \tag{4}$$

where X, Y, and Z are unknown constants to be determined by the boundary conditions. Since the electric potential at the valley is $\varphi|_{x=b/2,y=0} = \varphi_{\text{valley}}$, the values of Y and Z are

$$Y = \frac{\pi}{b},\ Z = \varphi_{\text{valley}}. \tag{5}$$

Matsushita *et al*. [35] revealed that the flux of lithium ions, J, was proportional to the electric potential gradient:

$$J \propto \frac{d\varphi}{dn} \approx E_0\left\{1 + X\frac{\pi}{b}\exp\left[-\frac{\pi}{b}y\right]\cos\left(\frac{\pi}{b}x\right)\right\}. \tag{6}$$

Thus, the ratio of fluxes at the peak and valley, J_{peak} and J_{valley}, can be expressed as

$$\frac{J_{\text{peak}}}{J_{\text{valley}}} = 1 + X\frac{\pi}{b}\exp\left[-\frac{\pi}{b}a\right]. \tag{7}$$

Take the equilibrium potential as zero for the reference state. Based on the Butler-Volmer equation, the electrochemical potential change at the valley can be expressed as

$$\Delta\mu^c{}_{\text{valley}} = -\frac{RT}{\alpha_a}\ln\frac{i}{i_0}. \tag{8}$$

After being combined with Eq. (4), the electrochemical potential change at the peak is given by

$$\Delta\mu^c{}_{\text{peak}} = \Delta\mu^c{}_{\text{valley}} - zF(\varphi_{\text{peak}} - \varphi_{\text{valley}}) = \Delta\mu^c{}_{\text{valley}} - zFE_0\left[a - X\exp\left(-\frac{\pi}{b}a\right)\right]. \tag{9}$$

Thus, the ratio of electrochemically related potential change at the peak and valley, $\Delta\mu^c{}_{\text{peak}}$ and $\Delta\mu^c{}_{\text{valley}}$, is

$$\frac{\Delta\mu^c{}_{\text{peak}}}{\Delta\mu^c{}_{\text{valley}}} = 1 + \frac{zFE_0}{\Delta\mu^c{}_{\text{valley}}}\left[X\exp\left(-\frac{\pi}{b}a\right) - a\right]. \tag{10}$$

The electrochemical potential is approximately proportional to ionic flux under a small current density. Thus,

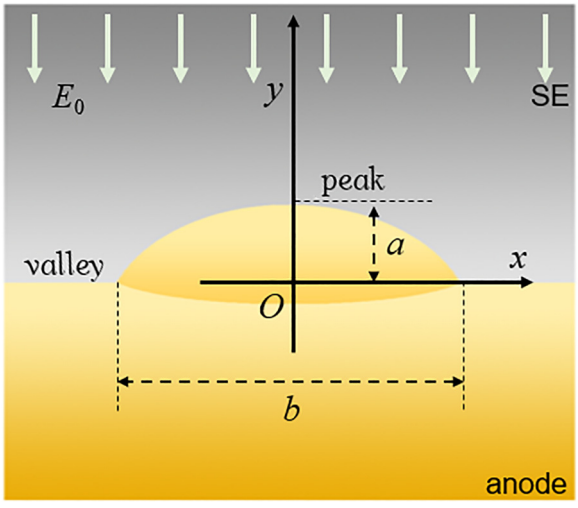

FIG. 2. Schematic of electrodeposition at the interface with a defect.

the relationship between chemical potential change and ion flux at the peak and valley satisfies [36]

$$\frac{\Delta\mu^{c}{}_{\text{peak}}}{\Delta\mu^{c}{}_{\text{valley}}} = \frac{J_{\text{peak}}}{J_{\text{valley}}}. \tag{11}$$

Substituting Eqs. (7) and (10) into Eq. (11) gives the value of X:

$$\begin{aligned} X &= \frac{a}{1-(\pi\mu^{c}{}_{\text{valley}}/zFbE_0)}\exp\left(\frac{\pi}{b}a\right) \\ &= \frac{a}{1-(\pi\eta^{c}{}_{\text{valley}}/bE_0)}\exp\left(\frac{\pi}{b}a\right). \end{aligned} \tag{12}$$

Typically, in solid-state batteries, the electric field, E_0, is as large as about 10^5–10^6 V/m; the defect size is about 10^{-6} m; and the overpotential, $\eta^{c}{}_{\text{valley}}$, is as small as about 10^{-2} V. For simplicity, the term $(\pi\eta^{c}{}_{\text{valley}}/bE_0) \approx 0.1$ is negligible, and the difference in $\Delta\mu^{c}$ at the peak and valley can be approximated as

$$\Delta\mu^{c}{}_{\text{peak}} - \Delta\mu^{c}{}_{\text{valley}} \approx \frac{\pi a}{b}\Delta\mu^{c}{}_{\text{valley}} = -\frac{\pi a}{b\alpha_a}RT\ln\frac{i}{i_0}. \tag{13}$$

Since the current density is larger than the exchange current density during electrodeposition, Eq. (13) implies that the electrochemically related variation, $\Delta\mu^{c}$, gives rise to unstable electrodeposition, $\Delta\mu^{c}_{\text{peak}} - \Delta\mu^{c}_{\text{valley}} < 0$.

In solid-state batteries, the potential change associated with the mechanical effect, $\Delta\mu^{m}$, corresponds to the change in the mechanical deformation energy of the system due to electrodeposition reactions. Based on the work-energy principle, the change in mechanical deformation energy equals the work done by interfacial stress without taking account of the dissipative energy. Thus, $\Delta\mu^{m}$ is given by

$$\begin{aligned} \Delta\mu^{m} &= \frac{\partial(W_{\text{anode}} + W_{\text{SE}})}{\partial n} \\ &= -\frac{\partial}{\partial n}\left(\int_{V_{\text{anode}}}^{V_{\text{anode}}+(\partial V_{\text{anode}}/\partial n)n}\sigma^{\Gamma}_{\text{anode}}dV\right. \\ &\quad \left. -+\int_{V_{\text{SE}}}^{V_{\text{SE}}+(\partial V_{\text{SE}}/\partial n)n}\sigma^{\Gamma}_{\text{SE}}dV\right), \\ &= -\sigma^{\Gamma}_{\text{anode}}\frac{\partial V_{\text{anode}}}{\partial n} - \sigma^{\Gamma}_{\text{SE}}\frac{\partial V_{\text{SE}}}{\partial n}, \end{aligned} \tag{14}$$

where n is the amount of reaction; W_{anode} and W_{SE} are the work done at the anode and the SE by interfacial stress, respective; V_{anode} and V_{SE} are the volumes of the anode and the SE, respectively; and $\sigma^{\Gamma}_{\text{anode}}$ and $\sigma^{\Gamma}_{\text{SE}}$ are the normal stresses of the anode and the SE at the interface, respectively. During the electrodeposition process, metal ions transfer from the SE to the anode, which gives

$$\frac{\partial V_{\text{anode}}}{\partial n} = V_{\text{M}}, \frac{\partial V_{\text{SE}}}{\partial n} = -V_{\text{M}^{z+}}, \tag{15}$$

where V_{M} is the molar volume of the anode; $V_{\text{M}^{z+}}$ is the molar volume of M^{z+} in the SE. We assume that the normal stress of the anode and the SE at the interface is continuous (i.e., $\sigma^{\Gamma}_{\text{anode}} = \sigma^{\Gamma}_{\text{SE}} = \sigma^{\Gamma}$). Thus, Eq. (14) can be rewritten as

$$\Delta\mu^{m} = -\sigma^{\Gamma}(V_{\text{M}} - V_{\text{M}^{z+}}). \tag{16}$$

The difference in potential change at the peak and valley can be expressed as

$$\Delta\mu^{m}{}_{\text{peak}} - \Delta\mu^{m}{}_{\text{valley}} = -(\sigma^{\Gamma}_{\text{peak}} - \sigma^{\Gamma}_{\text{valley}})(V_{\text{M}} - V_{\text{M}^{z+}}), \tag{17}$$

where $\sigma^{\Gamma}_{\text{peak}}$ and $\sigma^{\Gamma}_{\text{valley}}$ are the normal stresses of the peak and valley at the interface, respectively. It has been reported that the peak stress is much larger than the valley stress due to the stress concentration at the tip, and the maximum stress at the peak is the material strength of the SE. Thus, the difference in $\Delta\mu^{m}$ at the peak and valley can be simplified as

$$\Delta\mu^{m}{}_{\text{peak}} - \Delta\mu^{m}{}_{\text{valley}} \le \frac{K_c}{\sqrt{\pi a}}|V_M - V_{M^{z+}}|, \tag{18}$$

where K_c is the mechanical fracture toughness of the SE; $|V_{\text{M}} - V_{\text{M}^{z+}}|$ denotes the absolute value, ensuring that the difference in the molar volume of the anode and SE remains positive.

Typically, for a polymer SE, $V_{\text{M}} - V_{\text{M}^{z+}} < 0$, the increasing volume of new deposits fails to offset the shrinking volume of the SE and results in tensile stress at the interface ($\sigma^{\Gamma} > 0$); for an inorganic SE, $V_{\text{M}} - V_{\text{M}^{z+}} > 0$, the increasing volume of new deposits overcompensates for the shrinking volume of the SE, leading to compressive stress at the interface ($\sigma^{\Gamma} < 0$). Thus, Eq. (18) indicates that the mechanically related change, $\Delta\mu^{m}$, always suppresses dendrite growth and ensures stable electrodeposition for both polymer and inorganic SEs, $\Delta\mu^{m}_{\text{peak}} - \Delta\mu^{m}_{\text{valley}} \ge 0$.

Equations (13) and (18) indicate that the resulting electrodeposition represents a balance between the electrochemically and mechanically related electrochemical potential changes (for more details, see Sec. I within the Supplemental Material [37]). Substituting Eqs. (13) and (18) into Eq. (3) gives the critical condition for stable electrodeposition:

$$\ln\frac{i_{\text{critical}}}{i_0} \le \frac{b\alpha_a}{a\pi RT}\frac{K_c}{\sqrt{\pi a}}|V_{\text{M}} - V_{\text{M}^{z+}}|, \tag{19}$$

where i_{critical} denotes the CCD for stable electrodeposition. Equation (19) reveals that the interfacial defect size,

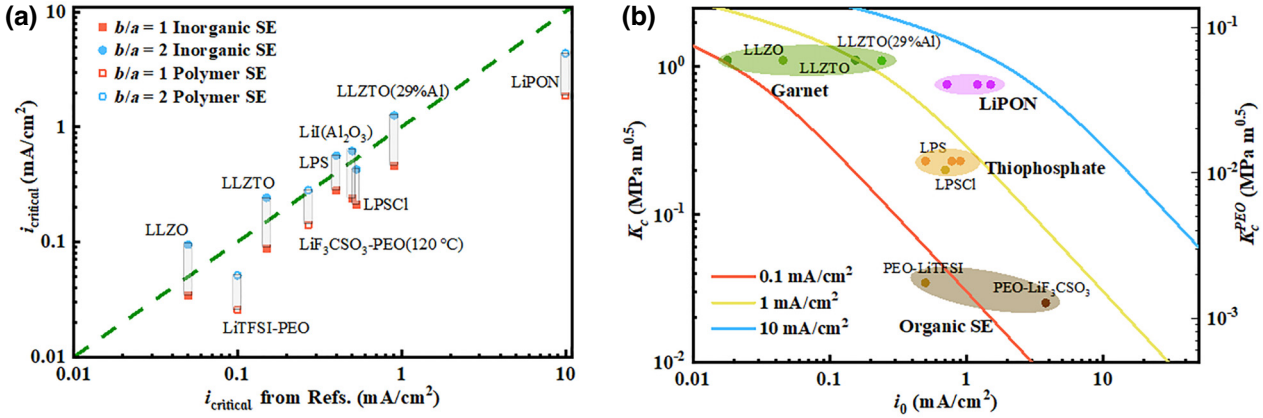

FIG. 3. (a) Comparison of the CCDs from theoretical and published results for typical SEs. (b) CCD map of typical SEs in terms of the fracture toughness and the exchange current density for a given defect size of $b/a = 2$.

material, and molar volume of the SE are fundamentally responsible for stable electrodeposition.

III. RESULTS AND DISCUSSION

To validate the robustness of the theoretical prediction, we take lithium-metal batteries with several representative SEs as examples. The physical parameters of various SEs used in the analyses are listed in Table S1 within the Supplemental Material [37]. Since the defect size of each SE is diverse and even unavailable in most existing works, we refer to reported data of surface defects in the garnet-type SE (i.e., LLZO), and select the same values (i.e., $b/a = 1$ and 2) for all the SEs in the calculations.

Figure 3(a) compares the predicted and experimental CCDs of typical SEs. For inorganic SEs [e.g., LLZO and Li_6PS_5Cl (LPSCl)], all the theoretical results are distributed around the diagonal, indicating that our theory provides excellent estimates of the CCDs, while, for polymer SEs (e.g., PEO), some quantitative differences between the predicted and published results can be observed. It is well known that polymer SEs have better interfacial contact with the anode than inorganic SEs, owing to their good shape flexibilities. Thus, adopting the same defect sizes as in inorganic SEs underestimates the predicted CCD values of polymer SEs.

Based on the criterion for stable electrodeposition, we conduct a CCD mapping of different SEs in terms of the fracture toughness and the exchange current density for a given defect size of $b/a = 2$ [Fig. 3(b)]. It shows that the garnet-type SEs and PEO-based polymer SEs fail to achieve stable electrodeposition under high current densities due to the low exchange current density and poor toughness, respectively. Only LiPON has the potential to meet the current density (10 mA/cm^2) required for the fast-charge goal of the Advanced Research Projects Agency-Energy [55]. The excellent fracture toughness and exceptional exchange current density make LiPON the only electrolyte reported so far that has been able to avoid dendrite penetration over extended cycling [56].

Equation (19) reveals that the interfacial defect is the main concern of stable electrodeposition for a given SE. To further explore the effect of defect size, *in situ* transmission electron microscopy (TEM) experiments are performed to observe dynamic electrodeposition at the Li|LLZO (Ta-doped) interface. The *in situ* TEM experiment is carried out inside an FEI Talos-F200s transition electron microscope at an accelerating voltage of 200 kV. The transition electron microscope is equipped with a TEM-STM holder, allowing for piezo-driven manipulation and electrical biasing. Ta-doped LLZO is selected as the representative SE. The density and ionic conductivity of sintered samples are 5.5 g cm^{-3} and 6.9×10^{-4} S cm^{-1}, respectively. In a glove box filled with Ar gas, a Cu rod attached to Li metal is pressed onto the LLZO particles, allowing it to semisubmerge in the Li metal. Then, the Cu rod is mounted on one end of the holder. On the other end, a Cu probe is mounted to serve as a working electrode, which is manipulated to form a contact with LLZO to assemble a solid-state battery. Finally, a constant bias voltage is applied to the Li metal counter electrode to initiate the Li deposition process, as shown in Fig. 4(a).

A Cu probe is in contact with LLZO to collect the current. Since the collected current is the local current at the defects in the experiments due to the point contact between the probe and LLZO, the corresponding average current density, i_{critical}, is obtained as $i_{\text{critical}} = I/S$, where I is the current collected by the probe and S is the contact area between the LLZO single crystal and lithium metal. The area of the selected LLZO crystal is estimated to be in the range of 39–125 μm^2. Thus, the contact area, S, is set as 80 μm^2.

Figures 4(b)–4(d) show that lithium metal gradually deposits and propagates laterally from the contact point

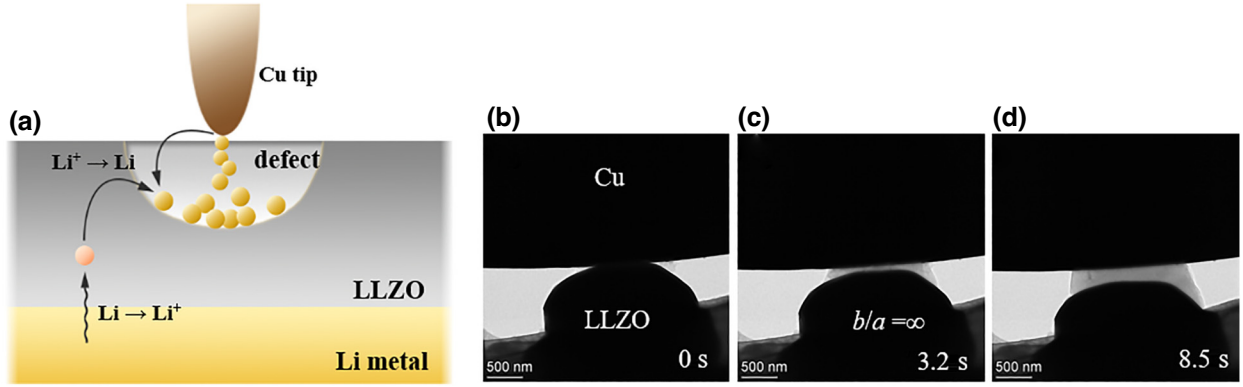

FIG. 4. (a) Schematic of electrodeposition at the Li|LLZO (Ta-doped) interface for *in situ* transmission electron microscopy observation. (b)–(d) Dynamic electrodeposition process at a perfectly defect-free surface ($b/a = \infty$).

when the copper tip is in contact with a perfectly defect-free surface ($b/a = \infty$). Even at a high average current density of 1 A/cm^2 (far larger than the CCD of LLZO in Refs. [26,27]), no dendrite is observed, and the cell remains uniformly deposited during the experiment.

Figure 5 shows the dynamic electrodeposition process with different defect sizes observed by *in situ* TEM, and the corresponding measured *I*-*t* curves. Detailed experimental results are listed in Table S2 within the Supplemental Material [37]. Taking the unstable electrodeposition case as an example [as shown in Fig. 5(a)], a Cu probe is initially brought into contact with an isolated LLZO particle and a high voltage of 3 V is applied at $t = 4$ s. Under the mechanical constraint, the rapid accumulation of lithium atoms leads to the generation of significant stress, which, in turn, gives rise to the abrupt formation of two defects ($b/a = 0.4$ and $b/a = 0.83$, as indicated by the outlined circle). This occurrence is accompanied by a prominent peak in the recorded *I*-*t* curve [depicted as the blue line in Fig. 5(b)]. In the presence of two initial defects, dendrite growth occurs gradually, accompanied by the opening of defects upon subsequent lithium intrusion. This phenomenon corresponds to another notable peak in the recorded *I*-*t* curve [depicted as the red line in Fig. 5(b)]. However, for the stable electrodeposition cases [Figs. 5(c) and 5(e)], no dendrites are observed, even under high current shocks [depicted as the blue lines in Figs. 5(d) and 5(f)], and the cell remains uniformly deposited during the experiment. In Fig. 5(g), despite a large current shock leading to the generation of an initial defect ($b/a = 3.3$) at $t = 2.4$ s, no dendrite penetration is observed under the subsequent applied current density [57] [depicted as the blue and red lines in Fig. 5(h)]. By summarizing the experimental results and relevant data, we create a stability diagram in terms of the CCD and the defect size (for more details, see Sec. III within the Supplemental Material [37]). It shows that the theoretical predictions agree well with the experimental observation that the CCD decays exponentially with the defect size.

Compared with single-crystal SEs, polycrystalline SEs are far more widely used in solid-state batteries, owing to their easy processability. Quantitatively estimating the effect of grain boundaries on the CCD is challenging through experimental means, because it is difficult to ensure the same roughness in SE samples to eliminate the effect of interfacial defects. Hence, we adopt molecular dynamics (MD) simulations to reveal the grain boundary effect on the CCD. Single-crystal and polycrystalline LLZO molecular models are established with sizes of 21×21 and 23×23 nm^2, respectively. To mimic the experimental procedure, an electric potential of 1.0 V/nm, corresponding to a current density of about 10^3 A/cm^2, is applied to drive lithium ions to deposit at the interface. Note that due to constraints in length and timescales within MD simulations, an exceptionally high current density, exceeding practical levels, is utilized to accelerate the electrodeposition process.

All MD simulations are performed by using the large-scale atomic-molecular massively parallel simulator package [58]. The interactions between the SE (LLZO) atoms are modeled with the Buckingham-Coulomb potential [59]; the interactions between Li-metal atoms are modeled with the second-nearest-neighbor embedded modified embedded-atom method (MEAM) force field [60]. The interactions between the atoms from lithium metal and LLZO are described using the universal force field [61]. Periodic boundary conditions are applied in the directions parallel to the initial dendrite, and the other direction is left as a free boundary. A virtual wall is added to the top and bottom of the system to limit its displacement in the *y* direction. MD simulations are performed in the *NPT* ensemble for the direction with periodic boundary conditions and the *NVT* ensemble with free boundary conditions; the temperature is set at 300 K. Lithium ions around the

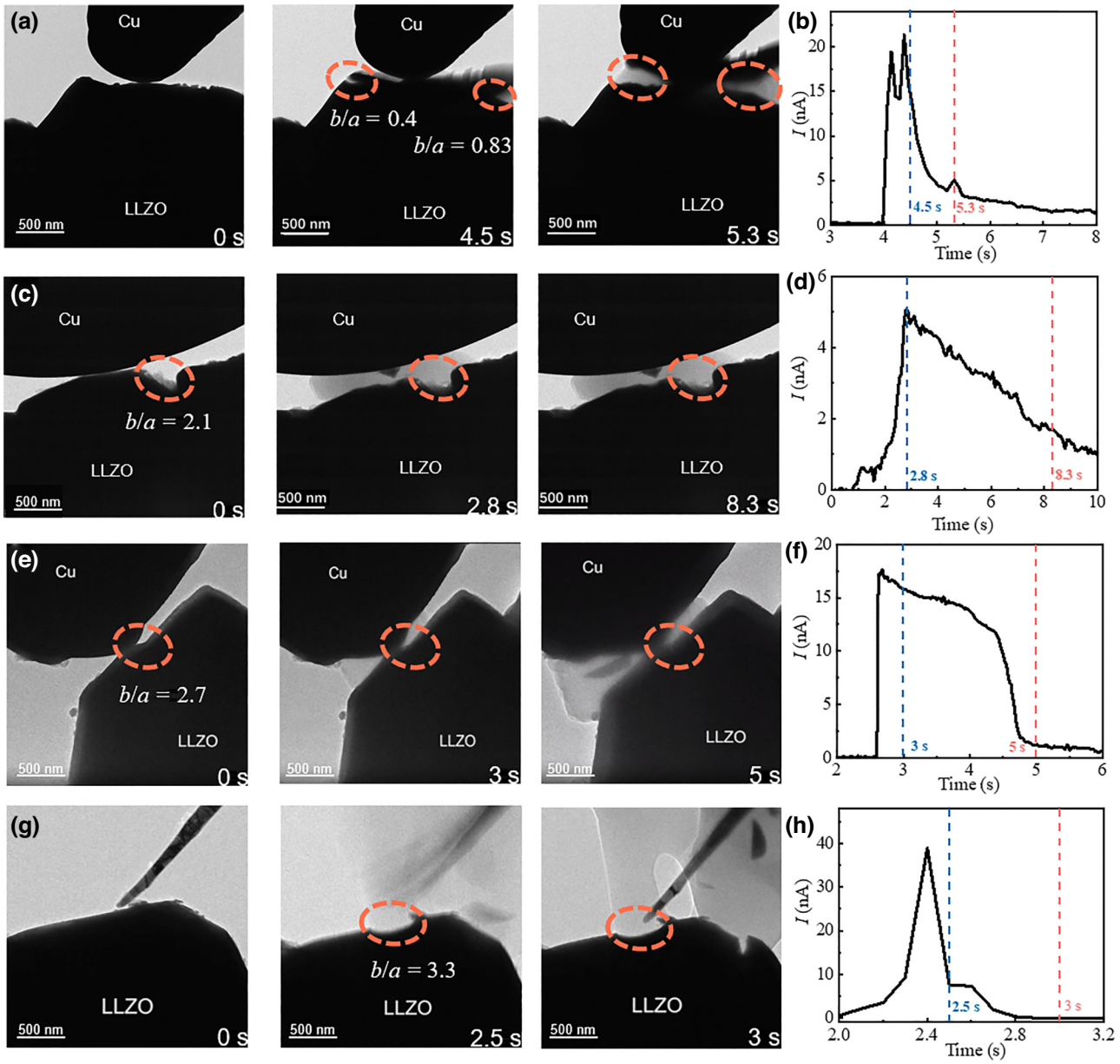

FIG. 5. Dynamic electrodeposition process with different defect sizes observed by *in situ* TEM, and the corresponding measured I-t curves. (a),(b) Unstable electrodeposition process with defect sizes of $b/a = 0.4$ and $b/a = 0.83$, and corresponding measured I-t curves; (c)–(h) Stable electrodeposition process with defect sizes of $b/a = 2.1$, $b/a = 2.7$, and $b/a = 3.3$, and the corresponding measured I-t curves.

lithium-metal atoms with a radius of 2 Å will be transformed into lithium-metal atoms to simulate the deposition process.

Figures 6(a) and 6(b) compare the electrodeposition behaviors in the single-crystal and polycrystalline SEs in the presence of the same preexisting defect size (i.e., $b/a = 2$). For the polycrystalline SE, the deposited lithium atoms are driven into the grain boundaries, initiating dendrite propagation; while for the single-crystal SE, the deposited lithium atoms prefer to plate the surface accompanied by stable electrodeposition. The different behaviors can be attributed to the inherent brittleness of grain boundaries. According to the MD simulation, with a defect size of 1.5 nm, the maximum stresses of single-crystal and polycrystalline LLZO under type I loading are 11.1 and 8.5 GPa, respectively. The type I fracture toughness, K_{IC}, can be calculated as [62]

$$K_{IC} = 1.12\sigma\sqrt{\pi a}. \tag{20}$$

The calculated fracture toughness of polycrystalline LLZO is 0.66 MPa $m^{0.5}$, about 22% loss of that compared

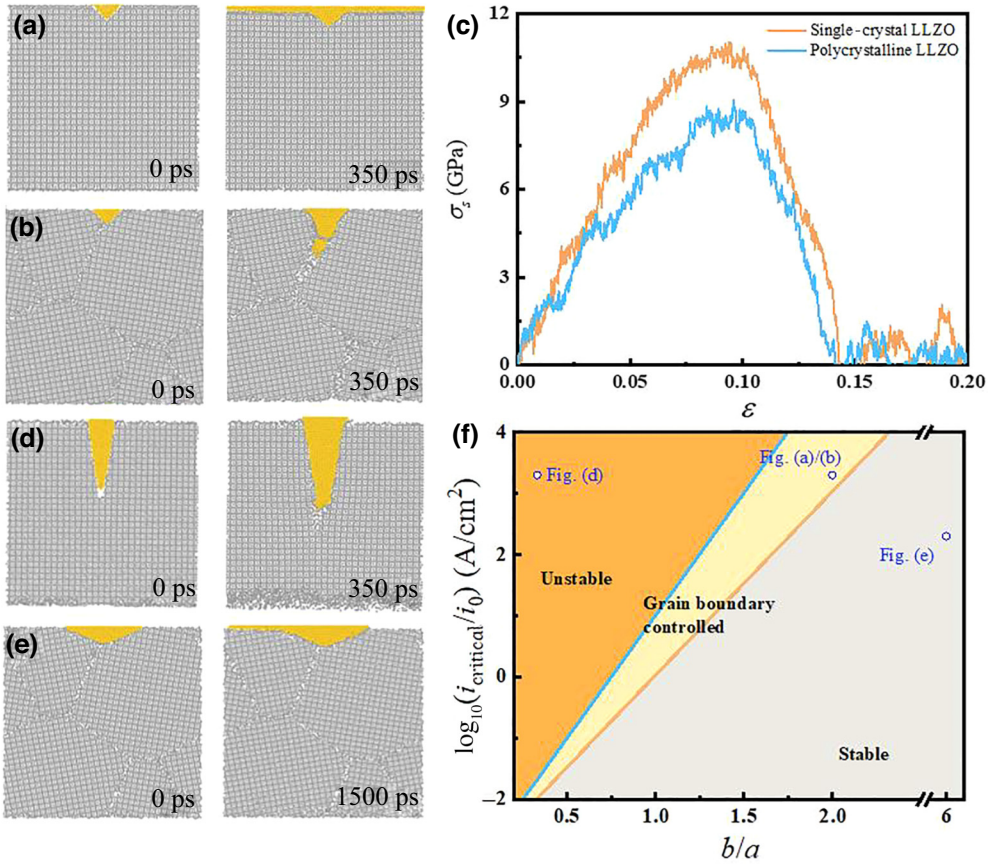

FIG. 6. (a),(b) Molecular dynamics simulations of electrodeposition at the interface for single-crystal and polycrystalline LLZO with the same defect size of $b/a = 2$, respectively. (c) Relationship between strain and stress of single-crystal and polycrystalline LLZO under type I loading. (d),(e) Molecular dynamics simulations of electrodeposition of single-crystal and polycrystalline LLZO with defect sizes of $b/a = 0.33$ and $b/a = 6$, respectively. (f) Stability diagram in terms of the CCD and defect size when considering the grain boundary effect.

to the single crystal [Fig. 6(c)], which, in turn, weakens the mechanical blocking effect, resulting in a reduced CCD.

Based on the simulated results and the obtained criterion [Eq. (19)], we construct a stability diagram, as shown in Fig. 6(f), in terms of the defect size and the current density ratio, i_{critical}/i_0. The stability diagram is divided into three regions. The stable region can be activated at a low charging rate with a small defect size [Fig. 6(e)], while the unstable region is the opposite [Fig. 6(d)]. Out of the two regions, there is an intermediate region controlled by the grain boundary, wherein it is possible to stabilize electrodeposition by replacing a polycrystalline SE with a single-crystal one. Note that the chemical composition of the LLZO surface plays a crucial role in its interaction and lattice compatibility with lithium metal, thereby influencing the deposition behavior of lithium ions. However, in this study, SE cracking is attributed to substantial pressure within dendrites, reaching up to 10 GPa. Under this immense pressure, lithium metal adopts an amorphous state, facilitating improved contact and lattice matching with various LLZO surfaces. This phenomenon ensures the stable deposition of lithium metal, effectively mitigating the impact of interfacial components.

In light of the above description, several design principles for the stabilization of metal electrodeposition in solid-state batteries have been proposed. First, with respect to the interface between the metal anode and SE, surface treatments that improve the adhesion of the metal anode to SEs are beneficial for lowering the interfacial defect size. In the same vein, mechanical polishing, applied stack pressure, and coating a thin buffer layer can also improve physical contact and promote stable electrodeposition. Similar arguments have also been mentioned in previous works [63], but, herein, we go a step further and reveal a quantitative relationship between the critical current density and the defect size. This is a significant step for the practical design of solid-state batteries. Second, with respect to the mechanical properties of the SE, it is wise to choose a SEs with high fracture toughness or increase the mechanical properties by carefully controlling the grain size, porosity, and preexisting cracks. Finally, polymer-inorganic composite electrolytes are preferable since the

rigid inorganic particles can improve the fracture toughness and the soft polymer matrix provides an outstanding interfacial compatibility with metal anodes.

IV. CONCLUSION

A theoretical model has been developed to bridge the gap between electrochemistry and mechanics in the electrodeposition of SEs to shed fresh light on our quantitative understanding of dendrite growth in SEs. A closed-form criterion for stable electrodeposition is given. In combination with *in situ* experiments and molecular simulations, the analysis shows that the defect size, partial molar volume, and the fracture toughness of the SE are fundamentally responsible for unstable electrodeposition. In addition, the low CCD of polycrystalline SEs is attributed to the inherent softening in toughness of grain boundaries. This work provides guidance for the rational design of solid-state batteries and suggests that minimizing the preexisting defect size is quite important for achieving outstanding performance.

ACKNOWLEDGMENTS

The authors gratefully acknowledge financial support from the National Natural Science Foundation of China, Grants No. 12002109, No. 12172102, and No. 52172240, and the Fundamental Research Funds for the Central Universities under Grant No. HIT.OCEF.2022013.

[1] Y. Lu, Z. Tu, and L. A. Archer, Stable lithium electrodeposition in liquid and nanoporous solid electrolytes, Nat. Mater. **13**, 961 (2014).

[2] M. Paunovic and M. Schlesinger, *Fundamentals of Electrochemical Deposition* (John Wiley & Sons, New York, 1988).

[3] D. Lin, Y. Liu, and Y. Cui, Reviving the lithium metal anode for high-energy batteries, Nat. Nanotechnol. **12**, 194 (2017).

[4] J. Zheng, Q. Zhao, T. Tang, J. Yin, C. D. Quilty, G. D. Renderos, *et al.*, Reversible epitaxial electrodeposition of metals in battery anodes, Science **366**, 645 (2019).

[5] B. Lee, E. Paek, D. Mitlin, and S. W. Lee, Sodium metal anodes: Emerging solutions to dendrite growth, Chem. Rev. **119**, 5416 (2019).

[6] P. Bai, J. Guo, M. Wang, A. Kushima, L. Su, J. Li, *et al.*, Interactions between lithium growths and nanoporous ceramic separators, Joule **2**, 2434 (2018).

[7] J. Zhang, Y. Liu, C. Wang, and H. Tan, An electrochemical-mechanical phase field model for lithium dendrite, J. Electrochem. Soc. **168**, 090522 (2021).

[8] Y. Liang, H. Dong, D. Aurbach, and Y. Yao, Current status and future directions of multivalent metal-ion batteries, Nat. Energy **5**, 646 (2020).

[9] L. S. de Vasconcelos, R. Xu, Z. Xu, J. Zhang, N. Sharma, S. R. Shah, J. Han, *et al.*, Chemomechanics of rechargeable batteries: Status, theories, and perspectives, Chem. Rev. **122**, 13043 (2022).

[10] T. Gao, D. Barnes, and W. Lu, Theory of Coupled Electrochemistry and Piezoelectricity in a Porous Medium, Phys. Rev. Lett. **128**, 068301 (2022).

[11] D. Cao, X. Sun, Q. Li, A. Natan, P. Xiang, and H. Zhu, Lithium dendrite in all-solid-state batteries: Growth mechanisms, suppression strategies, and characterizations, Matter **3**, 57 (2020).

[12] K. Takada, Progress and prospective of solid-state lithium batteries, Acta Mater. **61**, 759 (2013).

[13] F. Han, A. S. Westover, J. Yue, X. Fan, F. Wang, M. Chi, D. N. Leonard, *et al.*, High electronic conductivity as the origin of lithium dendrite formation within solid electrolytes, Nat. Energy **4**, 187 (2019).

[14] Z. Ahmad and V. Viswanathan, Stability of Electrodeposition at Solid-Solid Interfaces and Implications for Metal Anodes, Phys. Rev. Lett. **119**, 056003 (2017).

[15] A. Verma, H. Kawakami, H. Wada, A. Hirowatari, N. Ikeda, Y. Mizuno, T. Kotaka, *et al.*, Microstructure and pressure-driven electrodeposition stability in solid-state batteries, Cell Rep. Phys. Sci. **2**, 100301 (2021).

[16] Y. Lu, C. Zhao, H. Yuan, X. Cheng, J. Huang, and Q. Zhang, Critical current density in solid-state lithium metal batteries: Mechanism, influences, and strategies, Adv. Funct. Mater. **31**, 2009925 (2021).

[17] X. Han, Y. Gong, K. Fu, X. He, G. T. Hitz, J. Dai, A. Pearse, B. Liu, *et al.*, Negating interfacial impedance in garnet-based solid-state Li metal batteries, Nat. Mater. **16**, 572 (2016).

[18] L. Yang, H. S. Chen, H. Jiang, W. L. Song, and D. Fang, Lithium redistribution around the crack tip of lithium-ion battery electrodes, Scr. Mater. **167**, 11 (2019).

[19] F. Shen, M. B. Dixit, X. Xiao, and K. B. Hatzell, Effect of pore connectivity on Li dendrite propagation within LLZO electrolytes observed with synchrotron x-ray tomography, ACS Energy Lett. **3**, 1056 (2018).

[20] C. Monroe and J. Newman, The impact of elastic deformation on deposition kinetics at lithium/polymer interfaces, J. Electrochem. Soc. **152**, A396 (2005).

[21] T. Famprikis, P. Canepa, J. A. Dawson, M. S. Islam, and C. Masquelier, Fundamentals of inorganic solid-state electrolytes for batteries, Nat. Mater. **18**, 1278 (2019).

[22] Q. Tu, L. Barroso-Luque, T. Shi, and G. Ceder, Electrodeposition and mechanical stability at lithium-solid electrolyte interface during plating in solid-state batteries, Cell Rep. Phys. Sci. **1**, 100106 (2020).

[23] L. Porz, T. Swamy, B. W. Sheldon, D. Rettenwander, T. Frömling, H. L. Thaman, S. Berendts, *et al.*, Mechanism of lithium metal penetration through inorganic solid electrolytes, Adv. Energy Mater. **7**, 1701003 (2017).

[24] C. Yuan, X. Gao, Y. Jia, W. Zhang, Q. Wu, and J. Xu, Coupled crack propagation and dendrite growth in solid electrolyte of all-solid-state battery, Nano Energy **86**, 106057 (2021).

[25] D. S. Jolly, Z. Ning, J. E. Darnbrough, J. Kasemchainan, G. O. Hartley, P. Adamson, D. E. Armstrong, J. Marrow, and P. G. Bruce, Sodium/Na β" alumina interface: Effect of pressure on voids, ACS Appl. Mater. Interfaces **12**, 678 (2020).

[26] H. Liu, X. Cheng, J. Huang, H. Yuan, Y. Lu, C. Yan, G. Zhu, *et al.*, Controlling dendrite growth in solid-state electrolytes, ACS Energy Lett. **5**, 833 (2020).

[27] P. Barai, K. Higa, and V. Srinivasan, Lithium dendrite growth mechanisms in polymer electrolytes and prevention strategies, Phys. Chem. Chem. Phys. **19**, 20493 (2017).

[28] A. C. Luntz, J. Voss, and K. Reuter, Interfacial challenges in solid-state Li ion batteries, J. Phys. Chem. Lett. **6**, 4599 (2015).

[29] D. Bistri and C. V. Di Leo, A continuum electro-chemo-mechanical gradient theory coupled with damage: Application to Li-metal filament growth in all-solid-state batteries, J. Mech. Phys. Solids **174**, 105252 (2023).

[30] D. K. Singh, A. Henss, B. Mogwitz, A. Gautam, J. Horn, T. Krauskopf, S. Burkhardt, *et al.*, Li_6PS_5Cl microstructure and influence on dendrite growth in solid-state batteries with lithium metal anode, Cell Rep. Phys. Sci. **3**, 101043 (2022).

[31] M. Ganser, F. E. Hildebrand, M. Kamlah, and R. M. McMeeking, A finite strain electro-chemo-mechanical theory for ion transport with application to binary solid electrolytes, J. Mech. Phys. Solids **125**, 681 (2019).

[32] C. Monroe and J. Newman, The effect of interfacial deformation on electrodeposition kinetics, J. Electrochem. Soc. **151**, A880 (2004).

[33] L. Chen, H. W. Zhang, L. Y. Liang, Z. Liu, Y. Qi, P. Lu, J. Chen, and L. Q. Chen, Modulation of dendritic patterns during electrodeposition: A nonlinear phase-field model, J. Power Sources **300**, 376 (2015).

[34] L. Liang, Y. Qi, F. Xue, S. Bhattacharya, S. J. Harris, and L. Q. Chen, Nonlinear phase-field model for electrode-electrolyte interface evolution, Phys. Rev. E **86**, 051609 (2012).

[35] M. Matsushita, M. Sano, Y. Hayakawa, H. Honjo, and Y. Sawada, Fractal Structures of Zinc Metal Leaves Grown by Electrodeposition, Phys. Rev. Lett. **53**, 286 (1984).

[36] S. Fletcher and T. S. Varley, Beyond the Butler–Volmer equation. Curved Tafel slopes from steady-state current–voltage curves, Phys. Chem. Chem. Phys. **13**, 5359 (2011).

[37] See the Supplemental Material at http://link.aps.org/supplemental/10.1103/PRXEnergy.3.013010 for critical conditions for stable electrodeposition, material parameters of the solid electrolyte, detailed experimental results for Fig. 5, and a stability diagram in terms of the CCD and defect size. It also contains Refs. [15,24,26,38–54].

[38] H. Buschmann, S. Berendts, B. Mogwitz, and J. Janek, Lithium metal electrode kinetics and ionic conductivity of the solid lithium ion conductors "$Li_7La_3Zr_2O_{12}$" and $Li_{7-x}La_3Zr_{2-x}Ta_xO_{12}$ with garnet-type structure, J. Power Sources **206**, 236 (2012).

[39] X. Ke, Y. Wang, G. Ren, and C. Yuan, Towards rational mechanical design of inorganic solid electrolytes for all-solid-state lithium ion batteries, Energy Storage Mater. **26**, 313 (2020).

[40] X. Ke, Y. Wang, L. Dai, and C. Yuan, Cell failures of all-solid-state lithium metal batteries with inorganic solid electrolytes: Lithium dendrites, Energy Storage Mater. **33**, 309 (2020).

[41] T. R. Jow and C. C. Liang, Interface between solid electrode and solid electrolyte—a study of the $Li/LiI(Al_2O_3)$ solid-electrolyte system, J. Electrochem. Soc. **130**, 737 (1983).

[42] S. R. Ponnekanti, *Corrosion of Anodized Aluminum Alloys in Plasma Halide Chemistry* (The University of Texas at Austin, Austin, 1996).

[43] Y. Z. Sun, J. Q. Huang, C. Z. Zhao, and Q. Zhang, A review of solid electrolytes for safe lithium-sulfur batteries, Sci. China Chem. **60**, 1508 (2017).

[44] S. Sarkar and V. Thangadurai, Critical current densities for high-performance all-solid-state Li-metal batteries: Fundamentals, mechanisms, interfaces, materials, and applications, ACS Energy Lett. **7**, 1492 (2021).

[45] M. C. Pang, Y. Hao, M. Marinescu, H. Wang, M. Chen, and G. J. Offer, Experimental and numerical analysis to identify the performance limiting mechanisms in solid-state lithium cells under pulse operating conditions, Phys. Chem. Chem. Phys. **21**, 22740 (2019).

[46] V. Raj, N. P. B. Aetukuri, and J. Nanda, Solid state lithium metal batteries–issues and challenges at the lithium-solid electrolyte interface, Curr. Opin. Solid State Mater. Sci. **26**, 100999 (2021).

[47] F. Yue, Q. Xia, Y. Gong, M. Wang, H. Xia, and X. Huang, A fully coupled electrochemical-mechanical-thermal model of all-solid-state thin-film Li-ion batteries, J. Power Sources **539**, 231614 (2022).

[48] D. M. Pesko, Z. Feng, S. Sawhney, J. Newman, V. Srinivasan, and N. P. Balsara, Comparing cycling characteristics of symmetric lithium-polymer-lithium cells with theoretical predictions, J. Electrochem. Soc. **165**, A3186 (2018).

[49] S. Chakraborty, G. K. Sethi, L. Frenck, A. S. Ho, I. Villaluenga, H. Wantanabe, and N. P. Balsara, Effect of yield stress on stability of block copolymer electrolytes against lithium metal electrodes, ACS Appl. Energy Mater. **5**, 852 (2021).

[50] B. Guo, Y. Fu, J. Wang, Y. Gong, Y. Zhao, K. Yang, S. Zhou, L. Liu, S. Yang, X. Liu, and F. Pan, Strategies and characterization methods for achieving high performance PEO-based solid-state lithium-ion batteries, Chem. Commun. **58**, 8182 (2022).

[51] W. S. Loo, K. I. Mongcopa, D. A. Gribble, A. A. Faraone, and N. P. Balsara, Investigating the effect of added salt on the chain dimensions of poly(ethylene oxide) through small-angle neutron scattering, Macromolecules **52**, 8724 (2019).

[52] C. A. C. Sequeira and A. Hooper, The study of lithium electrode reversibility against (PEO)xLiF3CSO3 polymeric electrolytes, Solid State Ionics **9**, 1131 (1983).

[53] A. Hooper and J. M. North, The fabrication and performance of all solid state polymer-based rechargeable lithium cells, Solid State Ionics **9**, 1161 (1983).

[54] C. Li, P. Xue, L. Chen, J. Liu, and Z. Wang, Reducing the crystallinity of PEO-based composite electrolyte for high performance lithium batteries, Composites, Part B **234**, 109729 (2022).

[55] F. Han, A. S. Westover, J. Yue, X. Fan, F. Wang, M. Chi, D. N. Leonard, N. J. Dudney, H. Wang, and C. Wang, High electronic conductivity as the origin of lithium dendrite formation within solid electrolytes, Nat. Energy **4**, 187 (2019).

[56] A. S. Westover, N. J. Dudney, R. L. Sacci, and S. Kalnaus, Deposition and confinement of Li metal along an artificial Lipon–Lipon interface, ACS Energy Lett. **4**, 651 (2019).

[57] H. Gao, X. Ai, H. Wang, W. Li, P. Wei, Y. Cheng, S. Gui, H. Yang, Y. Yang, and M. Wang, Visualizing the failure of solid electrolyte under GPa-level interface stress induced by lithium eruption, Nat. Commun. **13**, 5050 (2022).

[58] A. P. Thompson, H. M. Aktulga, R. Berger, D. S. Bolintineanu, W. M. Brown, P. S. Crozier, P. J. in 't Veld, A. Kohlmeyer, S. G. Moore, T. D. Nguyen, and R. Shan, LAMMPS - a flexible simulation tool for particle-based materials modeling at the atomic, meso, and continuum scales, Comput. Phys. Commun. **271**, 108171 (2022).

[59] M. J. Klenk and W. Lai, Finite-size effects on the molecular dynamics simulation of fast-ion conductors: A case study of lithium garnet oxide $Li_7La_3Zr_2O_{12}$, Solid State Ionics **289**, 143 (2016).

[60] Z. Cui, F. Gao, Z. Cui, and J. Qu, A second nearest-neighbor embedded atom method interatomic potential for Li–Si alloys, J. Power Sources **207**, 150 (2012).

[61] A. K. Rappé, C. J. Casewit, K. S. Colwell, W. A. Goddard III, and W. M. Skiff, UFF, a full periodic table force field for molecular mechanics and molecular dynamics simulations, J. Am. Chem. Soc. **114**, 10024 (1992).

[62] T. L. Anderson, *Fracture Mechanics: Fundamentals and Applications* (CRC press, Boca Raton, 2017).

[63] X. Ma and Y. Xu, Effects of polishing treatments on the interface between garnet solid electrolyte and lithium metal, Electrochim. Acta **441**, 141789 (2023).